







Anisotropic satellite accretion on to the Local Group with HESTIA

Alexandra Dupuy^{},^{1,2}* Noam I. Libeskind,³ Yehuda Hoffman,⁴ H  l  ne M. Courtois^{},²
Stefan Gottl  ber,³ Robert J. J. Grand^{},^{5,6} Alexander Knebe^{},^{7,8,9} Jenny G. Sorce,^{3,10} Elmo Tempel^{},^{11,12}
R. Brent Tully,¹³ Mark Vogelsberger^{}¹⁴ and Peng Wang^{3,15}

¹Korea Institute for Advanced Study, 85, Hoegi-ro, Dongdaemun-gu, Seoul 02455, Republic of Korea

²University of Lyon, UCB Lyon 1, CNRS/IN2P3, IUF, IP2I, F-69100 Lyon, France

³Leibniz-Institut für Astrophysik Potsdam (AIP), An der Sternwarte 16, D-14482 Potsdam, Germany

⁴*Racah Institute of Physics, Hebrew University, Jerusalem 91904, Israel*

⁵*Instituto de Astrofísica de Canarias, Calle Vía Láctea s/n, E-38205 La Laguna, Tenerife, Spain*

⁶*Departamento de Astrofísica, Universidad de La Laguna, Av. del Astrofísico Francisco Sánchez s/n, E-38206 La Laguna, Tenerife, Spain*

⁷Departamento de Física Teórica, Módulo 15, Facultad de Ciencias, Universidad Autónoma de Madrid, E-28049 Madrid, Spain

⁸Centro de Investigación Avanzada en Física Fundamental (CIAFF), Facultad de Ciencias, Universidad Autónoma de Madrid, E-28049 Madrid, Spain

⁹International Centre for Radio Astronomy Research, University of Western Australia, 35 Stirling Highway, Crawley, WA 6009, Australia

¹⁰ *Université Paris-Saclay, CNRS, Institut d'Astrophysique Spatiale, F-91405 Orsay, France*

¹¹*Tartu Observatory, University of Tartu, Observatooriumi 1, 61602 Tõravere, Estonia*

¹²Estonian Academy of Sciences, 10130 Kohtu 6, Tallinn, Estonia

¹³*Institute for Astronomy (IfA), University of Hawaii, 2680 Woodlawn Drive, HI 96822, USA*

¹⁴Department of Physics, Kavli Institute for Astrophysics and Space Research, Massachusetts Institute of Technology, Cambridge, MA 02139, USA

¹⁵Shanghai Astronomical Observatories, Shanghai 200030, China

Accepted 2022 August 26. Received 2022 August 23; in original form 2022 June 2

ABSTRACT

How the cosmic web feeds haloes, and fuels galaxy formation is an open question with wide implications. This study explores the mass assembly in the Local Group (LG) within the context of the local cosmography by employing simulations whose initial conditions have been constrained to reproduce the local environment. The goal of this study is to inspect whether the direction of accretion of satellites on to the Milky Way and Andromeda galaxies is related to the cosmic web. The analysis considers the three high-resolution simulations available in the HESTIA simulation suite, as well as the derived velocity shear and tidal tensors. We notice two eras in the LG accretion history, delimited by an epoch around $z \approx 0.7$. We also find that satellites can travel up to ~ 4 Mpc, relative to their parent halo before crossing its viral radius R_{200} . Finally, we observe a strong alignment of the infall direction with the axis of slowest collapse \mathbf{e}_3 of both tidal and shear tensors, implying satellites of the LG originated from one particular region of the cosmic web and were channeled towards us via the process of accretion. This alignment is dominated by the satellites that enter during the early infall era, i.e. $z > 0.7$.

Key words: galaxies: haloes – dark matter – large-scale structure of Universe – cosmology: theory.

1 INTRODUCTION

The cosmological principle states that the Universe is isotropic and homogeneous on large enough scales. This implies that there are no special places nor special directions in the Universe. Nevertheless, this is not the case on smaller scales, where we observe structures suggesting the existence of preferred directions, such as the Supergalactic plane, recognized by de Vaucouleurs (1956, 1975).

The notion of *cosmic web* (Bond, Kofman & Pogosyan 1996) describes the anisotropic mass assembly of matter. It represents a natural frame of reference, or a natural coordinate system, within which we can define infall and the assembly of matter. Hence, it allows us to identify preferred directions in the Universe as opposed to other techniques that may be sensitive to scale but are insensitive

to directions, such as the two-point correlation function. However, it has been showed that the two-point correlation function can be modified to account for this anisotropy (see Paz, Stasyszyn & Padilla 2008). Still, the cosmic web provides an essential framework for the study of galaxy and structure formation (see Hahn et al. 2007b; Cautun et al. 2014; Gouin, Bonnaire & Aghanim 2021).

The distribution of matter in the Universe can be classified into four components of the cosmic web, which are knots, filaments, sheets and voids. Several algorithms and methodologies have been developed to derive this classification, either based on observational data [e.g. multiscale morphology filter (Aragón-Calvo et al. 2007; Aragon-Calvo & Yang 2014); SpineWeb (Aragón-Calvo et al. 2010); local skeleton (Sousbie et al. 2008); FINE (González & Padilla 2010); DisPerSE (Sousbie 2011); T-Rex (Bonnaire et al. 2020); ORIGAMI (Falck, Neyrinck & Szalay 2012; Falck & Neyrinck 2015); minimal spanning tree (Alpaslan et al. 2014); Bisous (Tempel et al. 2014b, 2016); multistream web analysis (Ramachandra & Shandarin 2015);

* E-mail: adupuy@kias.re.kr

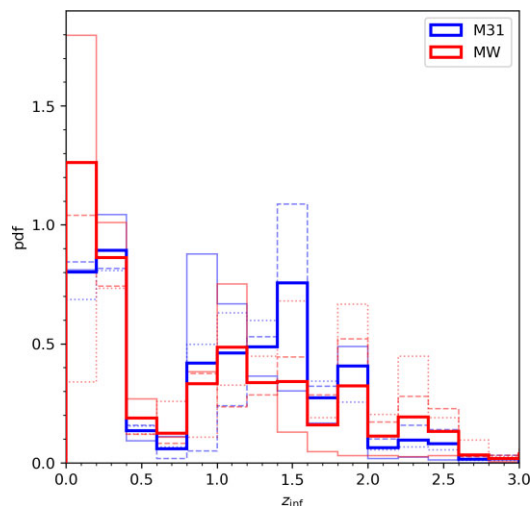


Figure 1. Distribution of redshifts at infall z_{inf} of all satellites that went through $2R_{200}$ of M31 (blue) or the MW (red), quantified as a probability distribution function. Thin solid, dashed, and dotted lines represent each one realization of the LG. The bold solid lines give the total infall redshift distribution, merging all three simulations.

and Lagrangian classifiers (Leclercq et al. 2017)], or numerical data [e.g. Hessian-based methods (Hahn et al. 2007a); the tidal shear tensor (Forero-Romero et al. 2009); the velocity shear tensor (Hoffman et al. 2012); CLASSIC (Kitaura & Angulo 2012); or NEXUS (Cautun, van de Weygaert & Jones 2013)]. A few of these methods have been brought together and compared in Libeskind et al. (2018).

Considering the notion of cosmic web as a description of the anisotropic mass assembly of matter, Libeskind et al. (2014) showed that the preferential direction of subhalo accretion is aligned with the axis of weakest collapse of the velocity shear tensor. Tempel et al. (2015) discussed the role of the cosmic web in the accretion of satellites using observational data from the Sloan Digital Sky Survey (SDSS; Aihara et al. 2011). Kang & Wang (2015) also studied subhalo accretion within the context of the cosmic web, focusing on the alignment with halo shape. Besides, Wang & Kang (2018) explored the correlation between the halo spin and the large-scale structures using the cosmic web, and later on showed that the spins of low-mass galaxies are preferentially aligned with the slowest collapsing direction, i.e. the eigenvector \mathbf{e}_3 of the tidal velocity field (Wang et al. 2018). In Welker et al. (2018), the authors aimed to explore the connection of the anisotropy of the spatial distribution of satellite galaxies to the local cosmic web. Finally, Wang et al. (2020b) considered group and filament data from SDSS and found that satellites are accreted along filaments (see also Gouin et al. 2020).

Many studies have related the infall pattern of satellites on to the Local Group (LG) to the flattened distribution of satellites of the Milky Way and Andromeda. Knebe et al. (2004) suggested that the origin of the flattened distribution of satellites is linked to a non-uniform infall pattern of accreted subhaloes. By examining the infall of subhaloes using a constrained simulation of the LG, hence reproducing the essential properties of the LG, Libeskind et al. (2011) showed that satellites galaxies tend to be accreted from preferred directions, rather than being accreted uniformly in all directions in the sky. Kubik et al. (2017) examined the difference in subhalo accretion between cold and warm dark matter cosmologies. Finally, Shao et al. (2018) studied the incidence of group and filamentary

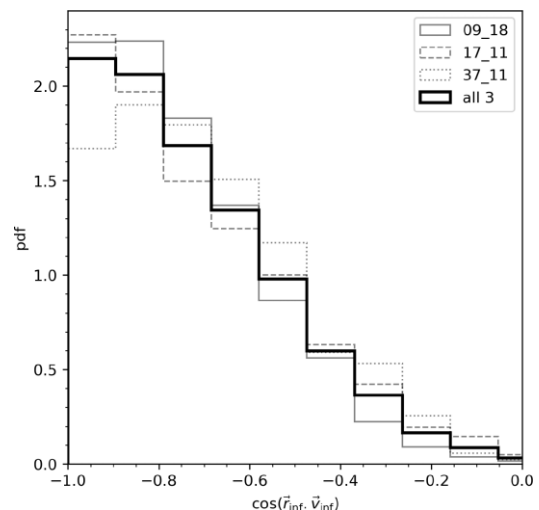


Figure 2. Distribution of the cosine of the angle between the direction of infall \mathbf{r}_{inf} and the velocity vector at infall \mathbf{v}_{inf} , by means of a probability distribution function. Thin solid, dashed, and dotted lines represent each one realization of the LG. The bold solid lines give the total infall redshift distribution, merging all three simulations.

dwarf galaxy accretion into the Milky Way, using hydrodynamical simulations, and found that the accretion of dwarf galaxies takes place preferentially perpendicular to the halo minor axis.

In this paper, we focus on investigating whether the preferential direction of subhalo accretion in the LG is related to the cosmic web and the local environment. We ask the questions: Are satellites in constrained simulations anisotropically accreted, and if so, are the directions co-incident with the local cosmic web? We will make use of the HESTIA simulations suite (Libeskind et al. 2020) and will consider satellites of both MW and M31. This paper is organized as followed. The methodology section, i.e. Section 2, describes the HESTIA simulations, the halo finder and the merger tree algorithms, as well as the cosmic web and the velocity shear and tidal tensors. The results of this paper are presented in Section 3. This paper ends with a short conclusion in Section 4, and Appendix A shows tests conducted on lower resolution simulations, which are also part of the HESTIA suite.

2 METHODS

2.1 HESTIA: simulations of the LG

The HESTIA simulation suite (Libeskind et al. 2020) is a set of low- and high-resolution cosmological magnetohydrodynamical simulations of the LG.

The *Cosmicflows-2* (CF2) peculiar velocities (Tully et al. 2013) are used to construct the initial conditions (within the framework of constrained simulations). The CF2 catalogue is grouped (Sorce & Tempel 2018) and bias-minimized (Sorce 2015). The simulations are built using the *AREPO* code to solve the ideal magnetohydrodynamics (MHD) equations (Springel 2010; Pakmor et al. 2016; Weinberger, Springel & Pakmor 2020), and the *AURIGA* galaxy formation model (Grand et al. 2017), which is based on the *Illustris* model (Vogelsberger et al. 2013) and implements various physical processes that are the most relevant for the formation and evolution of galaxies. Vogelsberger et al. (2014a,b) use the same galaxy formation model. The reader can also refer to Vogelsberger et al. (2020) for a review on cosmological simulations.

The entire suite of the HESTIA simulations assumes a Λ CDM cosmology with the following Planck Collaboration XVI (2014) values: $\sigma_8 = 0.83$, $H_0 = 100 h \text{ km s}^{-1} \text{ Mpc}^{-1}$, where $h = 0.677$, $\Omega_\Lambda = 0.682$, $\Omega_m = 0.270$, and $\Omega_b = 0.048$.

The publicly available AHF halo finder (Knollmann & Knebe 2009) identifies haloes, subhaloes, and their properties, at each redshift by detecting gravitationally bound particles. Structures containing less than 20 bound particles are not considered. Halo histories are derived by the MERGER TREE algorithm, a package included in the AHF software.

In this paper, we consider three LGs simulated at high resolution, namely 09_18, 17_11, and 37_11 (the numbers are based on the random seed used). These three simulations each consists of a region of two 3.7-Mpc spherical volumes centred on the two primary haloes at $z = 0$, filled with 8192^3 effective particles, achieving a mass and spatial resolution of $m_{\text{dm}} = 1.5 \times 10^5 M_\odot$, $m_{\text{gas}} = 2.2 \times 10^4 M_\odot$, and $\epsilon = 220 \text{ pc}$. A larger number of lower resolutions simulations are considered in the Appendix.

The reader may refer to Libeskind et al. (2020) for more details about the HESTIA suite and the algorithms mentioned above.

2.2 The cosmic web: velocity shear and tidal tensors

To evaluate the cosmic web, we consider the velocity shear tensor, derived from the distribution of the particles in the simulation box. First, a clouds-in-cell (CIC) technique is applied to the simulation to compute the density and velocity fields in a 256^3 grid of side length $100 \text{ Mpc } h^{-1}$, hence resulting in a spatial resolution of $0.39 \text{ Mpc } h^{-1}$. The grid is then smoothed with a Gaussian kernel, and various smoothing lengths $r_s = 1, 2, 5 \text{ Mpc } h^{-1}$ are considered.

Finally, the shear in the velocity field is derived from the velocity field as (Hoffman et al. 2012)

$$\Sigma_{\alpha\beta} = -\frac{1}{2H_0} \left(\frac{\partial V_\alpha}{\partial r_\beta} + \frac{\partial V_\beta}{\partial r_\alpha} \right), \quad (1)$$

where H_0 is the Hubble constant, and the partial derivatives of the velocity V are derived along the directions α and β , representing the orthogonal Supergalactic Cartesian axes x , y , and z . In each grid cell, we obtain the eigenvectors \mathbf{e}_1 , \mathbf{e}_2 , and \mathbf{e}_3 , and the corresponding eigenvalues ordered such that $\lambda_1 > \lambda_2 > \lambda_3$.

We also consider in this work the tidal shear tensor (Zel'Dovich 1970; Hahn et al. 2007a), defined as the Hessian of the gravitational potential ϕ :

$$T_{\alpha\beta} = -\frac{\partial^2 \phi}{\partial r_\alpha \partial r_\beta}, \quad (2)$$

where the gravitational potential is rescaled by a factor of $4\pi G \bar{\rho}$ (where G is the gravitational constant and $\bar{\rho}$ is the mean density of the Universe), and obeys the Poisson equation $\nabla^2 \phi = \delta$, where δ is the matter overdensity field.

Throughout this paper and for both tensors, the eigenvectors are computed following the methodology described in Wang et al. (2020a), which differs from the usual Nearest Grid Point method, as in this case the Hessian matrix is computed and solved for each halo in the simulation, instead of doing it once for the entire grid. In practice, the tensor fields are first evaluated on a grid. Instead of then begin evaluated on the grid, the method of Wang et al. (2020) computes a single tensor associated to each halo *before* diagonalization. The tensor field associated with each halo is constructed based on the seven adjoining cells in a CIC inspired way, namely weighted by the distance to the halo in consideration. Each halo thus has a unique

velocity or tidal tensor associated with it, which is then diagonalized and whose eigenvectors are then used.

2.3 Identifying accreted subhaloes

AHF uses the parameter R_{200}^1 to determine masses and radii of objects. In this case, the actual virial radius R_{vir} of haloes sits between R_{200} and $2R_{200}$. Hence, except when specifically mentioned, we consider the moment of infall at $2R_{200}$, as R_{vir} is larger than R_{200} and we do not expect much signal at that threshold (for reasons that will be explained and examined below).

Satellite galaxies are identified as being within R_{200} of their main host at $z = 0$. These are then tracked backwards in time by following the main branch of the merger tree, which tracks the location of the most massive progenitor (sub)halo. A moment of accretion is identified as when the satellite first crossed $2R_{200}$. This is termed z_{inf} . For clarity, we repeat that satellites are identified as those haloes that reside within R_{200} at $z = 0$ but their infall time is when they first crossed $2R_{200}$. This is because we are interested in examining the origin of the classical satellite population (not all LG dwarfs) and if their accretion happened at earlier times.

This is done by examining two adjacent snapshots. A subhalo is deemed to have been accreted if, in the later snapshot, it is located within a sphere of radius $2R_{200}$ centred on a main progenitor of one of the two LG haloes (MW or M31), where R_{200} is defined by the corresponding main progenitor. The progenitor of the subhalo has to be located outside of the so defined sphere at the earlier snapshot. By going backwards from $z = 0$ through all available snapshots, two at a time, we can follow the trajectories of satellites and identify the place and time of accretion. As mentioned earlier, only the subhaloes that survive up to $z = 0$ (i.e. the ones that are present within R_{200} in the $z = 0$ snapshot), are considered. Moreover, we only look at the first time the subhaloes cross the $2R_{200}$ threshold.

We refer to the time of infall as the last snapshot, corresponding to the redshift z_{inf} , before a given subhalo crosses for the first $2R_{200}$. We can then define the direction of infall \mathbf{r}_{inf} as the coordinates of the subhaloes at infall, re-centred on the respective main host (MW or M31). We also note the total mass of a subhalo at infall M_{200}^{inf} .

3 RESULTS

3.1 Properties of accretion on to the LG

The distribution of the redshifts z_{inf} , i.e. when the accreted subhaloes cross $2R_{200}$ of the MW (red lines) or M31 (blue lines), is shown in Fig. 1. The three LGs considered are represented by thin solid, dashed, or dotted lines (09_18, 17_11, and 37_11, respectively). The bold lines show the total redshift distribution of all satellites taken all together, for each main halo. Two peaks can be observed: late infall and early infall. The majority of satellites are accreted recently, after $z_{\text{inf}} = 0.7$. Other subhaloes get accreted much earlier $z_{\text{inf}} > 0.7$ and survive up to $z = 0$. Also, we observe that the three individual LGs show a similar trend. This demonstrates the quality and power of the constrained simulations, as such a behaviour would not be expected from randomly selected LGs. In fact, it has been previously established (Libeskind et al. 2010; Sorce et al. 2016; Carlesi et al. 2020) that one of the main traits of constrained simulations is that

¹The parameter R_{200} is defined as the radius at which the mean enclosed matter density is $\rho(< R_{200}) = 200 \times \rho_{\text{crit}}$, where ρ_{crit} corresponds to the critical density for closure.

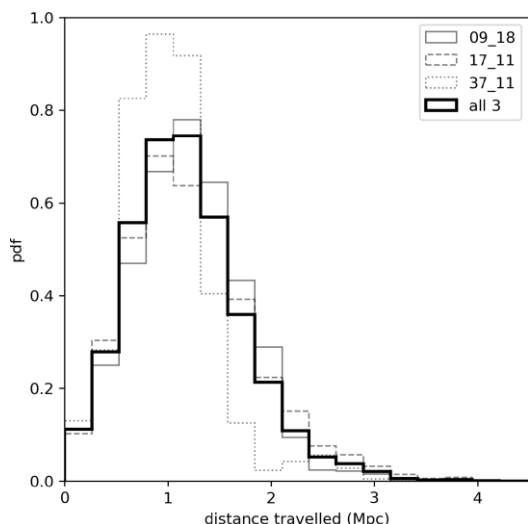


Figure 3. Distribution of the minimum distance travelled within the rest frame of the host, i.e. the distance in co-moving coordinates between the position at birth (at the first recorded snapshot) and the position at accretion, re-centred on the position of the main halo. The distribution is represented by a probability distribution function.

they limit the assembly histories of specific objects. We also note that both peaks of the distributions (total and for each LG) of the two main hosts overlap. This indicates that it is a feature of the entire LG, and that the haloes of the MW and M31 have likely had similar accretion histories.

Fig. 2 shows the distribution of the cosine of the angle between the infall direction \mathbf{r}_{inf} , vector at infall of the accreted satellite galaxy and the velocity vector at infall \mathbf{v}_{inf} . Both of these vectors are centred on the parent halo’s frame. Thin solid, dashed, and dotted lines correspond to a single realization of the LG. The bold solid lines gives the total distribution, combining all three simulations together. We can observe that the distribution peaks around $\cos(\mathbf{r}_{\text{inf}} \cdot \mathbf{v}_{\text{inf}}) = -1$, i.e. the two vectors are aligned with opposite direction, meaning that the satellites are accreted radially, along their velocity.

We can approximate the pre-infall distance travelled by satellites by considering the co-moving coordinate distance between their position at the first snapshot recorded (i.e. at *birth*) and their position at z_{inf} , both re-centred on the respective host halo. This approximation gives the minimum distance travelled by satellites before accretion, as we assume that their path from the birth to infall is a straight line, and do not consider their actual trajectories. The distribution of the distance travelled within the host rest frame, combining all three simulations, is shown in Fig. 3. We observe that subhaloes have travelled a distance up to 4 Mpc before getting accreted. More importantly, we notice a peak at 1 Mpc, showing that on average most $z = 0$ subhaloes traveled a distance of roughly 1 Mpc before crossing the $2R_{200}$ threshold of the MW or M31. That said, the median of the distribution is greater than this, implying that the LG accretes from, roughly, a sphere of up to 4 Mpc around the two main hosts.

In Fig. 4, the minimum co-moving distance travelled described above is plotted as a function of the redshift at the time of infall z_{inf} . Dark-matter-only haloes are represented by black dots, while haloes containing baryons are highlighted by red triangles. First, one can easily notice the two peaks in the redshift distribution as seen in Fig. 1, before and after $z = 0.7$. Moreover, the decreasing trend shows that the satellites accreted recently (recent z_{inf}) are the one that travelled the most, i.e. with the largest minimum travelled distance.

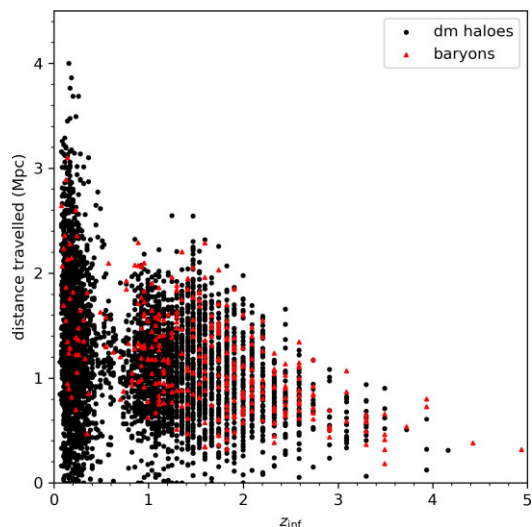


Figure 4. Minimum distance travelled as function of the redshift at infall z_{inf} . The blue and red square represent the dark matter and baryon-accreted subhaloes, respectively.

This is because the haloes that were recently accreted have had the most amount of time to travel across the Universe. Those accreted at early times had less time at their disposal and thus were not able to cross large distances.

3.2 Anisotropic infall within the context of the cosmic web

In this section, we analyse the alignment of the infall direction \mathbf{r}_{inf} with the three eigenvectors of the velocity shear and tidal tensors, by considering the distribution of the cosine of the angle between \mathbf{r}_{inf} and \mathbf{e}_1 , \mathbf{e}_2 , and \mathbf{e}_3 . As eigenvectors are non-directional, $0 \leq \cos(\mathbf{r}_{\text{inf}} \cdot \mathbf{e}_{1,2,3}) \leq 1$. A cosine of 1 means that the two directions are parallel while 0 implies they are perpendicular. To quantify the strength of the distribution of $\cos(\mathbf{r}_{\text{inf}} \cdot \mathbf{e}_{1,2,3})$, we calculate its statistical significance as the difference between the actual distribution and the median of 10 000 uniform distributions of the same size, averaged over all bins and calculated in units of the Poisson error. The uniform distributions are derived from 10 000 random samples of points uniformly distributed on a sphere. High values of the statistical significance indicate a strong deviation from a uniform distribution, hence a strong signal, while low values show a statistically weak signal, close to or consistent with a uniform distribution.

Fig. 5 shows the distribution of $\cos(\mathbf{r}_{\text{inf}} \cdot \mathbf{e}_{1,2,3})$ at R_{200} (top row) and $2R_{200}$ (bottom row). Note this is the only plot in the paper where we have examined the accretion at R_{200} . The three eigenvectors \mathbf{e}_1 , \mathbf{e}_2 , and \mathbf{e}_3 are represented, respectively, by blue, orange, and green lines. Both tidal and shear tensors have been checked; however, the obtained distributions being similar, only the tidal tensor eigenvectors are shown for clarity. Similarly, as all smoothing lengths applied to the tensors show similar trends, only the distributions obtained with a smoothing length of $r_s = 1$ Mpc are displayed. The left- to right-hand columns depict all satellites (combining all three simulations and both host haloes), MW satellites only, and M31 satellites only, respectively. The statistical significance of each distribution is noted on the top of each panel, with the same colour code as their respective eigenvector: blue for \mathbf{e}_1 , orange for \mathbf{e}_2 , and green for \mathbf{e}_3 . The grey-shaded regions depict the Poisson error, i.e. the standard deviation σ of 10 000 uniform distributions at each bin. The dark grey shows the $\pm 1\sigma$ interval, while the lighter grey shows the $\pm 2\sigma$ interval.

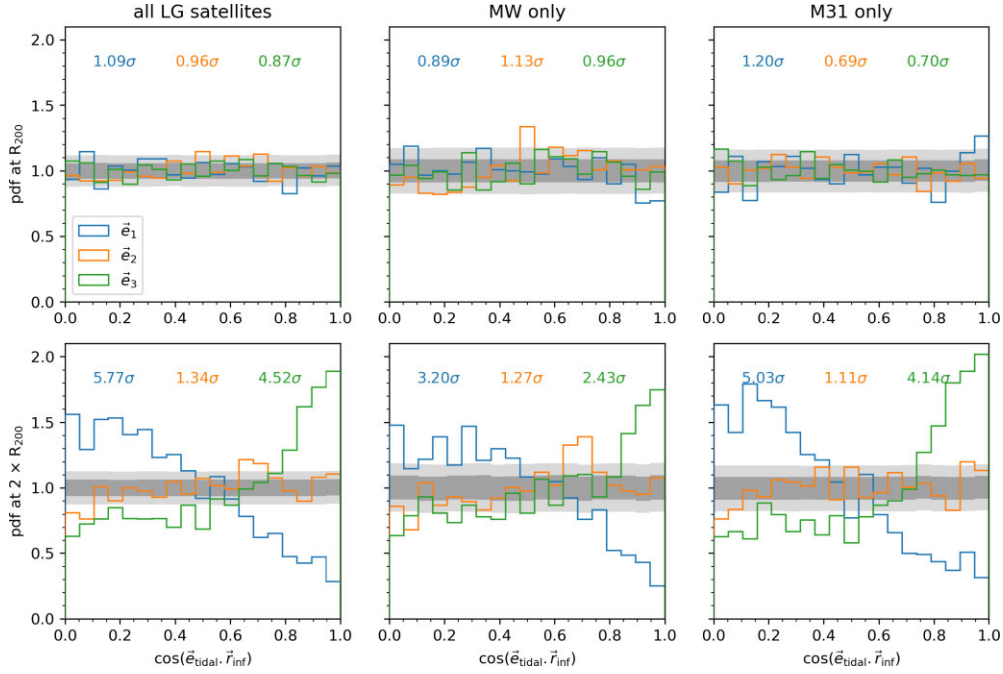


Figure 5. Distribution of the angles between the infall direction \mathbf{r}_{inf} at R_{200} (top row) and $2R_{200}$ (bottom row) and the three eigenvectors \mathbf{e}_1 (blue), \mathbf{e}_2 (orange), and \mathbf{e}_3 (green) of the tidal tensor, where a smoothing of 1 Mpc has been applied. All distributions are depicted by probability density distributions. The three columns depict the distribution of all accreted satellites (all three high-resolution simulations combined), MW satellites only and M31 satellites only, from the left- to right-hand side, respectively. The statistical significance of each distribution is depicted on the top of each panel, and is characterized by the average offset in each bin between the considered distribution and the median of 10 000 uniform ones, calculated in units of the Poisson error. The shaded light and dark grey region represent, respectively, the $\pm 1\sigma$ and $\pm 2\sigma$ thresholds, where σ is the standard deviation of 10 000 uniform distribution. The reader may check the corresponding text in the manuscript for more details.

The distributions in top row panels of Fig. 5 being mostly located within the grey regions, and the values of the statistical significance being mostly less or close to unity, indicate there is no significant alignment of the infall direction with any eigenvector of the tidal tensor. We remind the reader that the top row corresponds to the distribution of accreted subhaloes at R_{200} . However, when looking at the distributions at $2R_{200}$ in the bottom row panels of Fig. 5, we notice that the infall direction \mathbf{r}_{inf} is strongly aligned with the axis of slowest collapse \mathbf{e}_3 . We also notice that \mathbf{r}_{inf} is orthogonal to \mathbf{e}_1 , while no significant alignment is observed with \mathbf{e}_2 . At R_{200} , i.e. in the non-linear regime, the signal is extremely weak due to non-linear dynamics. Beyond R_{200} , we transition from the virial regime to the quasi-linear (QL) regime, which explains why the signal is much stronger at $2R_{200}$.

Besides, when comparing the middle (MW satellites) and right-hand (M31 satellites) columns of Fig. 5, corresponding to satellites accreted by each host separately, no significant difference can be observed in the top row, i.e. at R_{200} , for the same reasons described above. At $2R_{200}$, the distributions corresponding to both hosts look similar; however, the statistical significance corresponding to the satellites accreted by M31 is ~ 1.7 times higher than the one corresponding to the MW satellites. This shows that, although the alignment with \mathbf{e}_3 is observed for both hosts, it is stronger for M31, and weaker for the MW satellites. Such a difference may be explained by the fact that M31 is more massive than the MW.²

²The more massive haloes are called M31 by definition in HESTIA simulations.

In the next figures, we look at the distribution of $\cos(\mathbf{r}_{\text{inf}} \cdot \mathbf{e}_{1,2,3})$ at $2R_{200}$ split by the mass and redshift, in order to check for any dependence.

First, Fig. 6 shows the distribution of $\cos(\mathbf{r}_{\text{inf}} \cdot \mathbf{e}_{1,2,3})$ at $2R_{200}$, where $\mathbf{e}_{1,2,3}$ are represented by blue, orange, and green lines, respectively. For clarity purposes, only the results obtained from the tidal tensor, smoothed by 1 Mpc, are shown; however, both shear and tidal tensors show similar trends. Similarly, the results obtained with other smoothing lengths are not displayed as the distributions are very similar. The distributions are split by total mass of satellites at accretion, namely M_{200}^{inf} , using the following bins: $M_{200}^{\text{inf}} < 10^7$ (first column), $10^7 \leq M_{200}^{\text{inf}} < 10^8$ (second column), and $M_{200}^{\text{inf}} > 10^8$ M_{\odot} (third column). The statistical significance and the standard deviation of a uniform distribution are shown on each panel. The reader may refer to the previous figures for a detailed description. All three mass bins show alignment of the accretion; however, we observe a mild mass dependence wherein the smallest infall masses ($M_{200}^{\text{inf}} > 10^7 M_{\odot}$) exhibit a weaker signal than the more massive haloes. The $10^7 \leq M_{200}^{\text{inf}} < 10^8$ mass bin is stronger.

In Fig. 7, the distributions of $\cos(\mathbf{r}_{\text{inf}} \cdot \mathbf{e}_{1,2,3})$ at $2R_{200}$ are split into two bins of redshift at infall z_{inf} : late and early infall. Subhaloes accreted recently at $z_{\text{inf}} < 0.7$ are shown in the left-hand column, while the ones accreted earlier at $z_{\text{inf}} \geq 0.7$ are shown in the right-hand column. The top row shows the distribution with the tidal tensor's eigenframe, while the bottom rows show this distribution for the shear tensor. The reader may refer to the texts of the previous figures for a detailed description of the colour code and quantities displayed on the panels. We notice that the alignment with \mathbf{e}_3 is dominated by early infall and is more isotropic at later times.

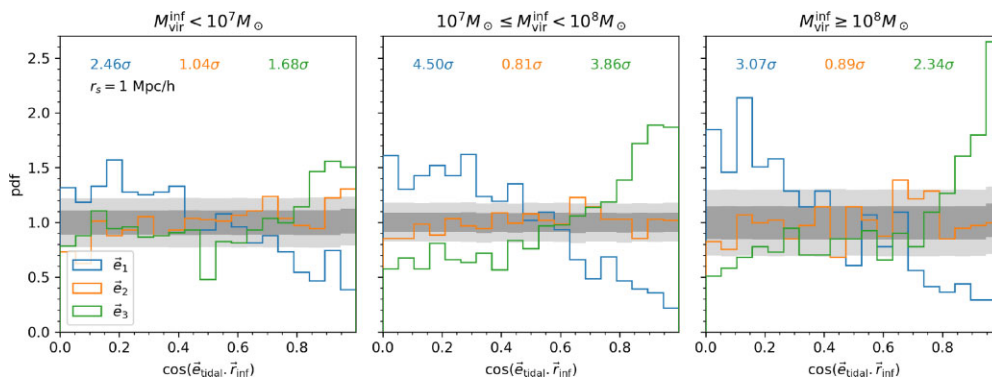


Figure 6. Distribution of $\cos(\mathbf{r}_{\text{inf}} \cdot \mathbf{e}_{1,2,3})$ at $2R_{200}$, split by the total mass of satellites at infall M_{200}^{inf} (first column: $M_{200}^{\text{inf}} < 10^7 M_{\odot}$, second column: $10^7 \leq M_{200}^{\text{inf}} < 10^8 M_{\odot}$, third column: $M_{200}^{\text{inf}} \geq 10^8 M_{\odot}$). The reader may refer to the caption of Fig. 5 for the description of the layout and the colour code of the different panels.

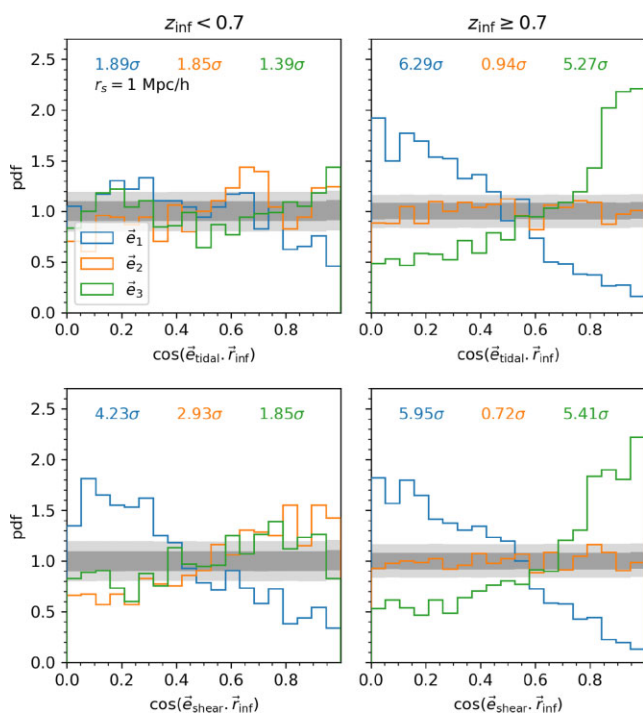


Figure 7. Distribution of $\cos(\mathbf{r}_{\text{inf}} \cdot \mathbf{e}_{1,2,3})$ at $2R_{200}$, split by redshift at infall (first column: $z_{\text{inf}} < 0.7$, second column: $z_{\text{inf}} \geq 0.7$). The upper row corresponds to the tidal tensor, while the bottom row corresponds to the shear tensor. The reader may refer to the caption of Fig. 5 for the description of the layout and the colour code of the different panels.

Finally, Fig. 8 depicts the location of the MW (left-hand panel) and M31 (right-hand panel) satellites entry points as they cross the $2R_{200}$ of their respective main halo. The entry points are shown as a ‘heat map’ and plotted on an Aitoff projection of the $2R_{200}$ sphere, oriented in the eigenframe of the tidal tensor, smoothed at 1 Mpc. As the eigenvectors are non-directional, only a single octant of the $2R_{200}$ sphere is shown, instead of an entire full-sky projection. The north pole of the projection corresponds to the direction of \mathbf{e}_1 , the right point on the horizontal axis at $+90^\circ$ corresponds to the direction of \mathbf{e}_2 , and the mid-point corresponds to the direction of \mathbf{e}_3 . Areas within 15° of the eigenvectors \mathbf{e}_1 , \mathbf{e}_2 , and \mathbf{e}_3 are defined, respectively, by blue, orange, and green circles. The yellow pixels correspond to a high density of satellite entry points, while dark blue pixels correspond

to a low density of entry points. The location of the simulated Virgo in all three realizations is shown as white scattered points (circle: 09_18, triangle: 17_11, square: 37_11). In both cases, we observe a high density of points around \mathbf{e}_3 , which is in accordance with the results shown above. Besides, the high density around the axis of slowest collapse looks more spherical in the case of M31 than for the MW, confirming the different trends between the two main hosts observed in the middle and right-hand panels of Fig. 5.

We remind the reader that Fig. 8 represents a single octant of the $2R_{200}$ sphere as eigenvectors are non-directional. However, one can give directions to the eigenvectors in order to get a full-sky representation of this sphere by choosing positive direction. We establish an oriented eigenframe with respect to Virgo, by choosing as positive, the direction of each eigenvector \mathbf{e}_1 , \mathbf{e}_2 , and \mathbf{e}_3 as the direction closest to the orientation of Virgo (effectively putting Virgo into the first octant of the coordinate system). This new setting of the eigenframe is shown in Fig. 9. Similarly to the previous Fig. 8, Fig. 9 shows the location of MW (left-hand panel) and M31 (right-hand panel) subhalo entry points as they cross the $2R_{200}$ threshold of their respective main host. The colourmap and coloured circles are the same as in 8. The red point and error bars correspond, respectively, to the mean and standard deviation of the locations of Virgo in the three simulations. As in Fig. 8, the infall pattern indicates that subhaloes appear to be accreted from the general direction of Virgo. Put another way, the \mathbf{e}_3 vector points towards Virgo.

4 CONCLUSION

This paper presents a study of the accretion of $z = 0$ satellites in the LG, in the context of the cosmic web. The analysis uses the high-resolution simulations available in the HESTIA simulation suite, constrained with the Cosmicflows-2 cosmography, and also considers the velocity shear and tidal tensors derived from the simulations, as they describe the anisotropic assembly of matter in the Universe. The main results of our study are the following:

- (i) We observe two eras in the LG history, corresponding to an early and a late infall, i.e. before and after $z \approx 0.7$. This gap is observed in all of the LG simulations we considered in this paper (both lower and higher resolutions).
- (ii) Most accreted satellites travel ~ 1 Mpc before crossing the R_{200} threshold of their respective main host. Some travel up to 4 Mpc.
- (iii) No significant alignment with the large-scale structure is observed at R_{200} , due to non-linear dynamics.

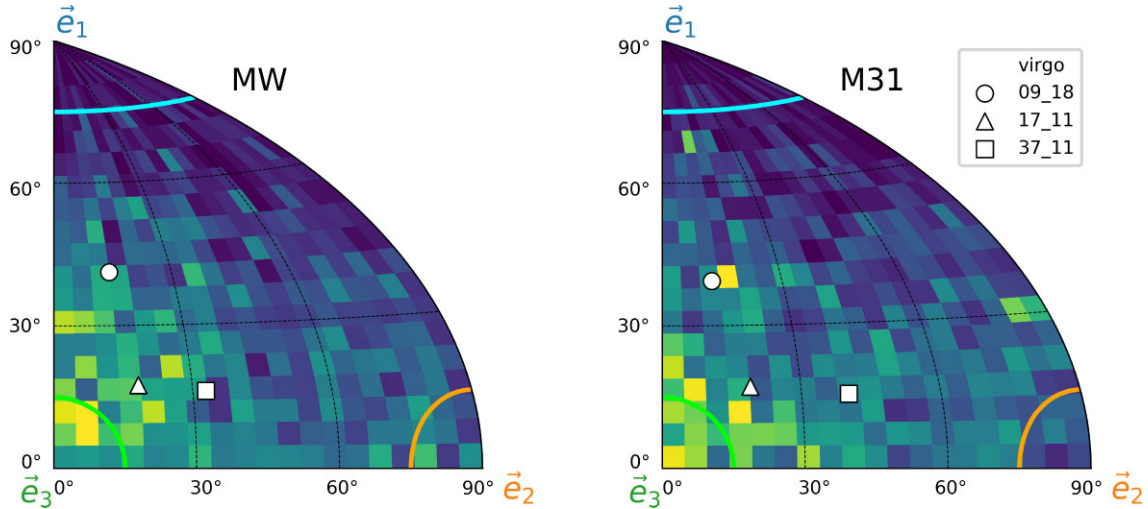


Figure 8. Location of MW (left-hand panel) and M31 (right-hand panel) satellites entry points as they cross the $2R_{200}$ threshold of their respective main host, shown as the density of points on an Aitoff projection. The projection is oriented in the frame of the tidal tensor eigenvectors smoothed at 7 Mpc, such that the north pole corresponds to the direction of e_1 , the right point on the horizontal axis at $+90^\circ$ corresponds to e_2 , and the mid-point corresponds to e_3 . The blue, orange and green circles define areas within 15° of the eigenvectors e_1 , e_2 , and e_3 , respectively. As the eigenvectors are non-directional, only a single octant of the sphere is shown. Yellow corresponds to a high density of satellite entry points, while dark blue corresponds to a low density of entry points. The location of Virgo simulated in all three realizations is shown as white scattered points (circle: 09_18, triangle: 17_11, square: 37_11).

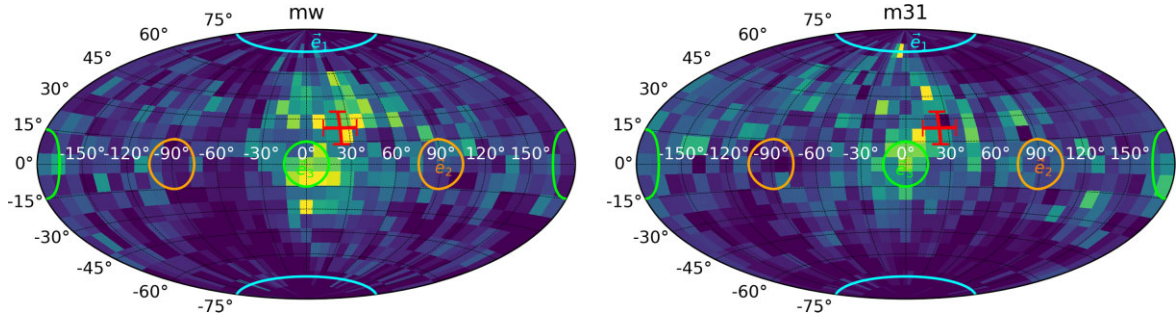


Figure 9. Fig. 8 shown as a full-sky projection by giving directions to the eigenframe with respect to Virgo. The colourmap corresponds to high (yellow) and low (blue) densities of MW (left-hand panel) and M31 (right-hand panel) subhalo entry points. Areas within 15° of the eigenvector are highlighted by blue (e_1), orange (e_2), and green (e_3) circles. The red point and error bars correspond, respectively, to the mean and standard deviation of the locations of Virgo in the three simulations.

(iv) The infall direction at $2R_{200}$ is strongly aligned with the eigenvector e_3 of both velocity shear and tidal tensors. $2R_{200}$ probes the transition from the non-linear to QL regimes.

(v) The alignment with e_3 is stronger for the M31 satellites than the MW satellites, as the statistical significance of the alignment is 1.7 times higher. This could be because the M31 halo is more massive and thus exerts more of an influence on the tidal field.

(vi) The alignment with e_3 is slightly stronger for large infall masses, especially within mass bin $10^7 \leq M_{200}^{\text{inf}} < 10^8$.

(vii) However, it has been shown that the alignment with the axis of slowest collapse is dominated by early infall ($z > 0.7$).

As mentioned previously in this paper, this analysis considers only the accreted subhaloes that survive up to $z = 0$ and are located within R_{200} of their host. Hence, the satellites that are not present in the last $z = 0$ snapshot (they may have been stripped and fell below the simulations resolution limit, or simply merged, but still cross the virial radius at some earlier time) are not considered in this study. As a perspective, one could go further with the analysis by considering

all accreted satellites in the LG history. This may allow to confirm the alignment of the preferred infall direction with the cosmic web, and look for other properties, while improving the statistics by increasing the number of considered satellites.

This paper has many cosmological implications, as we found evidence that the local cosmography has influence on the accretion of matter within the LG. The mass assembly in the LG is dictated by the cosmic web, more precisely the velocity shear and tidal tensors, within a range of influence of up to 4 Mpc. This means that what occurs to the LG is determined by what takes place within this range of 4 Mpc.

The preferred direction of accretion being aligned with the axis of slowest collapse e_3 shows that the mass being fed into the LG may come from a local filament, which itself should be aligned with e_3 as well (Tempel et al. 2014a). Besides, additionally to showing how the accreted subhaloes are arranged with respect to the eigenframe and the simulated Virgo cluster, the aitoff projections in Figs 8 and 9 also indicate where Virgo is located with respect to the eigenframe. In

particular, we notice that the direction of Virgo is close to the direction of e_3 . We may compare the results presented in this paper with Shaya & Tully (2013) and Shaya et al. (2017). Those studies concern the formation of the local environment using numerical action orbit reconstructions, which are based on the same Cosmicflows data constraints as the HESTIA high-resolution simulations considered in this paper. Specifically, Shaya & Tully (2013) focus on the formation details of the LG. We know from their stellar populations that most dwarf galaxies formed very early. Additionally, today, a large part of these are located within planar structures. In the large volume that the numerical action method models, Shaya & Tully (2013) found that the motion of the LG (shared by MW and M31) is predominantly towards $-SGZ$ and $+SGY$ (in Supergalactic Cartesian coordinates), i.e. aligned with the directions of the e_1 and e_3 eigenvectors, respectively. The authors also found that most of the dwarf galaxies are being drawn into the M31 halo oriented in the plane of the e_2 and e_3 , favouring e_3 , which is consistent with the main result of our paper. Shaya & Tully (2013) also state that the LG satellites have a common origin, as most of them evacuate from the Local Void. In our case, we are not looking specifically at the Local Void, but we do observe that satellites come from a specific direction. Shaya et al. (2017) concentrate on the large-scale aspects of the LG formation, particularly illustrating the importance of the expansion of the Local Void in the development of the Local Sheet (i.e. establishing the compressive eigenvector direction e_1) and the attractive influence of the Virgo Cluster (i.e. establishing the expansive eigenvector direction e_3). The infall pattern towards M31 and MW is not aligned with the Local Void, but aligned with the Local Sheet. So, first satellites evacuate from the Local Void to the Local Sheet, then from the Local Sheet to the LG. This is consistent both with our intuition that material collapses along e_1 first and e_3 last, as well as previous work that shows this (Kang & Wang 2015). Tracking back the material that forms satellites at this level is out of scope for this paper, as we only focus on the direction of accretion of MW and M31 within the context of the cosmic web, and not looking at throughout the orbital history of the accreted satellites, from the Local Void to the Local Sheet and the LG.

Finally, the study presented in this paper might offer a framework regarding the peculiar geometric spatial distribution of satellites in the LG. The identification of a preferred direction, with respect to the cosmic web and the cosmography, and a range of influence of the LG, could provide support in addressing this issue.

ACKNOWLEDGEMENTS

This work has been done within the framework of the Constrained Local UniversE Simulations (CLUES) simulations. AD is supported by a KIAS Individual Grant (PG087201) at Korea Institute for Advanced Study. YH has been partially supported by the Israel Science Foundation grant ISF 1358/18. ET acknowledges support by ETAg grant PRG1006 and by the EU through the ERDF CoE grant TK133. AK is supported by the Ministerio de Ciencia, Innovación y Universidades (MICIU/FEDER) under research grant PGC2018-094975-C21 and further thanks Claudine Longet for nothing to lose. HC is grateful to the Institut Universitaire de France and CNES for its support. JS acknowledges support from the French Agence Nationale de la Recherche for the LOCALIZATION project under grant agreements ANR-21-CE31-0019. The authors gratefully acknowledge the Gauss Centre for Supercomputing e.V. (<http://www.gauss-centre.eu>) for funding this project by providing computing time on the GCS Supercomputer SuperMUC at Leibniz Supercomputing Centre (<http://www.lrz.de>).

DATA AVAILABILITY

The data used in this work were extracted from the HESTIA simulation suite. Requests for access to the HESTIA simulation data should be directed to the CLUES collaboration and will be made available upon reasonable request.

REFERENCES

- Aihara H. et al., 2011, *ApJS*, 193, 29
 Alpaslan M. et al., 2014, *MNRAS*, 438, 177
 Aragon-Calvo M. A., Yang L. F., 2014, *MNRAS*, 440, L46
 Aragon-Calvo M. A., Jones B. J. T., van de Weygaert R., van der Hulst J. M., 2007, *A&A*, 474, 315
 Aragon-Calvo M. A., Platen E., van de Weygaert R., Szalay A. S., 2010, *ApJ*, 723, 364
 Bond J. R., Kofman L., Pogosyan D., 1996, *Nature*, 380, 603
 Bonnaire T., Aghanim N., Decelle A., Douspis M., 2020, *A&A*, 637, A18
 Carlesi E., Hoffman Y., Gottlöber S., Libeskind N. I., Knebe A., Yepes G., Pilipenko S. V., 2020, *MNRAS*, 491, 1531
 Cautun M., van de Weygaert R., Jones B. J. T., 2013, *MNRAS*, 429, 1286
 Cautun M., van de Weygaert R., Jones B. J. T., Frenk C. S., 2014, *MNRAS*, 441, 2923
 de Vaucouleurs G., 1956, *Vistas Astron.*, 2, 1584
 de Vaucouleurs G., 1975, *ApJ*, 202, 610
 Falck B., Neyrinck M. C., 2015, *MNRAS*, 450, 3239
 Falck B. L., Neyrinck M. C., Szalay A. S., 2012, *ApJ*, 754, 126
 Forero-Romero J. E., Hoffman Y., Gottlöber S., Klypin A., Yepes G., 2009, *MNRAS*, 396, 1815
 González R. E., Padilla N. D., 2010, *MNRAS*, 407, 1449
 Gouin C., Aghanim N., Bonjean V., Douspis M., 2020, *A&A*, 635, A195
 Gouin C., Bonnaire T., Aghanim N., 2021, *A&A*, 651, A56
 Grand R. J. J. et al., 2017, *MNRAS*, 467, 179
 Hahn O., Porciani C., Carollo C. M., Dekel A., 2007a, *MNRAS*, 375, 489
 Hahn O., Carollo C. M., Porciani C., Dekel A., 2007b, *MNRAS*, 381, 41
 Hoffman Y., Metuki O., Yepes G., Gottlöber S., Forero-Romero J. E., Libeskind N. I., Knebe A., 2012, *MNRAS*, 425, 2049
 Kang X., Wang P., 2015, *ApJ*, 813, 6
 Kitaura F.-S., Angulo R. E., 2012, *MNRAS*, 425, 2443
 Knebe A., Gill S. P. D., Gibson B. K., Lewis G. F., Ibata R. A., Dopita M. A., 2004, *ApJ*, 603, 7
 Knollmann S. R., Knebe A., 2009, *ApJS*, 182, 608
 Kubik B., Libeskind N. I., Knebe A., Courtois H., Yepes G., Gottlöber S., Hoffman Y., 2017, *MNRAS*, 472, 4099
 Leclercq F., Jasche J., Lavaux G., Wandelt B., Percival W., 2017, *J. Cosmol. Astropart. Phys.*, 2017, 049
 Libeskind N. I., Yepes G., Knebe A., Gottlöber S., Hoffman Y., Knollmann S. R., 2010, *MNRAS*, 401, 1889
 Libeskind N. I., Knebe A., Hoffman Y., Gottlöber S., Yepes G., Steinmetz M., 2011, *MNRAS*, 411, 1525
 Libeskind N. I., Knebe A., Hoffman Y., Gottlöber S., 2014, *MNRAS*, 443, 1274
 Libeskind N. I. et al., 2018, *MNRAS*, 473, 1195
 Libeskind N. I. et al., 2020, *MNRAS*, 498, 2968
 Pakmor R., Springel V., Bauer A., Mocz P., Munoz D. J., Ohlmann S. T., Schaal K., Zhu C., 2016, *MNRAS*, 455, 1134
 Paz D. J., Stasyszyn F., Padilla N. D., 2008, *MNRAS*, 389, 1127
 Planck Collaboration et al., 2014, *A&A*, 571, A16
 Ramachandra N. S., Shandarin S. F., 2015, *MNRAS*, 452, 1643
 Shao S., Cautun M., Frenk C. S., Grand R. J. J., Gómez F. A., Marinacci F., Simpson C. M., 2018, *MNRAS*, 476, 1796
 Shaya E. J., Tully R. B., 2013, *MNRAS*, 436, 2096
 Shaya E. J., Tully R. B., Hoffman Y., Pomarède D., 2017, *ApJ*, 850, 207
 Sorce J. G., 2015, *MNRAS*, 450, 2644
 Sorce J. G., Tempel E., 2018, *MNRAS*, 476, 4362
 Sorce J. G., Gottlöber S., Hoffman Y., Yepes G., 2016, *MNRAS*, 460, 2015
 Sousbie T., 2011, *MNRAS*, 414, 350

- Sousbie T., Pichon C., Courtois H., Colombi S., Novikov D., 2008, *ApJ*, 672, L1
- Springel V., 2010, *MNRAS*, 401, 791
- Tempel E., Libeskind N. I., Hoffman Y., Liivamägi L. J., Tamm A., 2014a, *MNRAS*, 437, L11
- Tempel E., Stoica R. S., Martínez V. J., Liivamägi L. J., Castellan G., Saar E., 2014b, *MNRAS*, 438, 3465
- Tempel E., Guo Q., Kipper R., Libeskind N. I., 2015, *MNRAS*, 450, 2727
- Tempel E., Stoica R. S., Kipper R., Saar E., 2016, *Astron. Comput.*, 16, 17
- Tully R. B. et al., 2013, *AJ*, 146, 86
- Vogelsberger M., Genel S., Sijacki D., Torrey P., Springel V., Hernquist L., 2013, *MNRAS*, 436, 3031
- Vogelsberger M. et al., 2014a, *MNRAS*, 444, 1518
- Vogelsberger M. et al., 2014b, *Nature*, 509, 177
- Vogelsberger M., Marinacci F., Torrey P., Puchwein E., 2020, *Nat. Rev. Phys.*, 2, 42
- Wang P., Kang X., 2018, *MNRAS*, 473, 1562
- Wang P., Guo Q., Kang X., Libeskind N. I., 2018, *ApJ*, 866, 138
- Wang P., Kang X., Libeskind N. I., Guo Q., Gottlöber S., Wang W., 2020a, *New Astron.*, 80, 101405
- Wang P., Libeskind N. I., Tempel E., Pawłowski M. S., Kang X., Guo Q., 2020b, *ApJ*, 900, 129
- Weinberger R., Springel V., Pakmor R., 2020, *ApJS*, 248, 32
- Welker C., Dubois Y., Pichon C., Devriendt J., Chisari N. E., 2018, *A&A*, 613, A4
- Zel'Dovich Y. B., 1970, *A&A*, 500, 13

APPENDIX: TESTS

In order to gauge convergence of the results shown here, tests have been carried out on lower resolution simulations. Throughout this section, we consider 13 lower resolution Local Group simulations, filled with 4096^3 effective particles, instead of 8192^3 as in the main body of the paper. Due to the lower resolution, we expect to identify fewer accreted satellites. However, with more simulations, we hope to make up for the lack of resolution. The other parameters stay unchanged, so the reader may refer to Section 2.1 for a detailed reminder of the simulations parameters. The lower resolution simulations have dark matter particles mass of $1.2 \times 10^6 M_\odot$, gas mass of $1.8 \times 10^5 M_\odot$, and a softening of 340 pc. This means that fewer satellites per host halo are resolved. A total of 1883 satellites (774 MWs and 1109 M31s) are identified in the 4096 simulation, against 4486 (2122 MWs and 2364 M31s) satellites in the higher resolution one.

The results obtained from the simulation with 4096^3 particles are plotted in dashed lines in Figs A1 and A2, corresponding, respectively, to Fig. 1 and the bottom left-hand panel of Fig. 5. They are compared to the results presented in this paper, represented in bold lines, and corresponding to the bold lines as well in both Figs 1 and 5 (bottom left-hand panel).

In both figures, we observe similar patterns between the two resolutions. More importantly, Fig. A2 shows that the alignment of the infall with the axis of slowest collapse e_3 , present in the higher resolution results, can still be noticed in the lower resolution simulation.

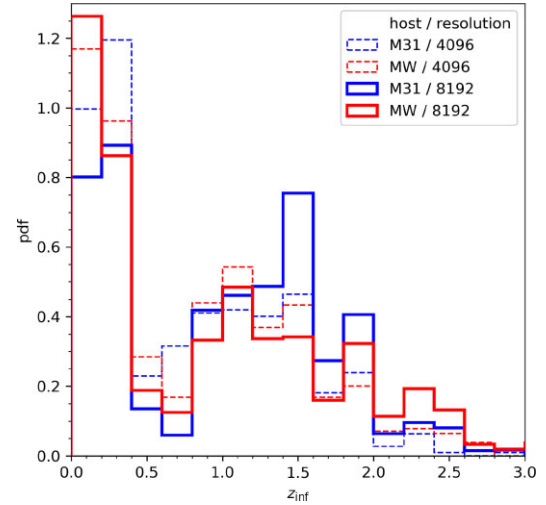


Figure A1. Distribution of redshifts at infall z_{inf} of all satellites that went through $2R_{200}$ of M31 (blue) or the MW (red) as a probability density function. Thin dashed lines represent the simulation with a lower resolution (4096). The bold solid lines gives the results obtained from the higher resolution simulation (8192), i.e. the bold lines in Fig. 1. In both cases, all realizations considered are merged.

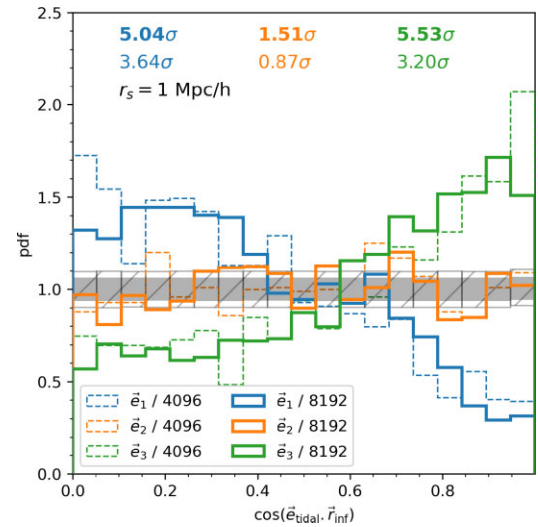


Figure A2. Distribution of the angles between the infall direction r_{inf} at $2R_{200}$ and the three eigenvectors e_1 , e_2 , and e_3 of the tidal tensor on which a smoothing of $r_s = 1$ Mpc/h has been applied. Distributions are quantified by means of probability density functions. The reader may refer to the caption of Fig. 5 for the description of the layout and the colour code. Thin dashed lines represent the results given by the simulation with a lower resolution (4096), while the bold solid lines gives the results obtained from the higher resolution simulation (8192), i.e. the bold lines in the bottom left-hand panel of Fig. 5. In both cases, all realizations considered are merged. For clarity purposes, only the regions corresponding to the $\pm 1\sigma$ threshold are shown, where the hatched one corresponds to the lower resolution simulation, and the one filled in grey corresponds to the higher resolution simulation.

This paper has been typeset from a \LaTeX file prepared by the author.